JOM, Vol. 67, No. 5, 2015
DOI: 10.1007/s11837-015-1356-1
© 2015 The Minerals, Metals & Materials Society

On the Development of a Zinc Vapor Condensation Process for the Solar Carbothermal Reduction of Zinc Oxide

N. TZOUGANATOS,[1] M. DELL'AMICO,[2] C. WIECKERT,[1] J. HINKLEY,[2] and A. STEINFELD[3,4]

1.—Solar Technology Laboratory, Paul Scherrer Institute, 5232 Villigen, Switzerland. 2.—CSIRO Energy Centre, Mayfield West, Newcastle, NSW 2304, Australia. 3.—Department of Mechanical and Process Engineering, ETH Zurich, 8092 Zurich, Switzerland. 4.—e-mail: aldo.steinfeld@ethz.ch

In the conventional Imperial Smelting Process, the dominating pyrometallurgical zinc production process, zinc vapor is recovered from the furnace off-gas by absorption into an intense spray of molten lead droplets in a splash condenser, followed by separation of zinc from the Zn-Pb alloy upon cooling from 550°C to 450°C by taking advantage of the decrease in the solubility of zinc in lead at lower temperatures. The adaptation of this condenser technology into a solar-driven thermochemical plant using concentrated solar energy faces several drawbacks owing to its mechanical complications and the continuous recirculation of large quantities of lead. An alternative zinc condenser concept involving gas bubbling through a zinc liquid bath of the off-gas evolved from the carbothermal reduction of ZnO is thus proposed and numerically modeled for transient heat and mass transfer. Condensation of bubbles containing 53.5% of noncondensable gases yielded chemical conversions of Zn(g) to Zn(l) in the range of 95.6–99.8% for operation in the temperature range 500–650°C while conversions of Zn(g) to ZnO in the order of 10^{-6} were obtained, thus predicting successful suppression of Zn(g) reoxidation by CO_2 and CO.

INTRODUCTION

Zinc is produced from the reduction of ZnO via either the electrolytic or the pyrometallurgical processing routes.[1–3] In the dominating pyrometallurgical process, the Imperial Smelting Furnace (ISF) process,[4] Zn is extracted in a blast furnace by carbothermally reducing ZnO to form Zn(g) and CO in a highly endothermic reaction according to:

$$\begin{aligned} &\mathrm{ZnO(s)} + \mathrm{C(s)} = \mathrm{Zn(g)} + \mathrm{CO} \\ &\Delta H^{\circ}_{298\,K} = 239.9\,\mathrm{kJ\,mol^{-1}} \end{aligned} \tag{1}$$

The predominant reaction route is via the solid–gas reaction:

$$\begin{aligned} &\mathrm{ZnO(s)} + \mathrm{CO} = \mathrm{Zn(g)} + \mathrm{CO_2} \\ &\Delta H^{\circ}_{298\,K} = 67.5\,\mathrm{kJ\,mol^{-1}} \end{aligned} \tag{2}$$

where CO is formed by the Boudouard reaction:

$$\begin{aligned} &\mathrm{CO_2} + \mathrm{C(s)} = 2\ \mathrm{CO} \\ &\Delta H^{\circ}_{298\,\mathrm{K}} = 172.4\,\mathrm{kJ\,mol^{-1}} \end{aligned} \tag{3}$$

The heat required to drive the reaction is provided by the exothermic combustion of coke in preheated air entering into the furnace bosh.

Integration of concentrated solar energy into pyrometallurgical processes as an alternative energy source could significantly contribute to carbon dioxide mitigation in the production of zinc metal.[5] The use of high-temperature solar process heat for the carbothermal reduction of ZnO has been previously proposed and experimentally demonstrated using a novel indirectly irradiated packed-bed solar reactor concept on a laboratory (10 kW_{th})[6,7] and pilot plant (300 kW_{th}) scale.[8,9] In addition to primary Zn production, zinc recovery from secondary sources via the carbothermal reduction of solar-purified Waelz oxide has also been experimentally investigated on a 10 kW_{th} scale.[10] Furthermore, the

(Published online March 11, 2015)

use of methane as an alternative carbonaceous reducing agent for the co-production of Zn and synthesis gas by the combined reduction of ZnO and reforming of CH_4 has been proposed and tested using a 5 kW_{th} vortex-flow solar reactor prototype.[11]

As the process temperatures in pyrometallurgical Zn production far exceed its boiling point (1180 K), it is produced in the vapor phase. Zinc vapor then has to be rapidly condensed (Eq. 4) to prevent the reoxidation reactions (Eqs. 5 and 6) to proceed:

$$\mathrm{Zn(g)} = \mathrm{Zn(l)} \tag{4}$$

$$\mathrm{Zn(g)} + \mathrm{CO_2} = \mathrm{ZnO(s)} + \mathrm{CO} \tag{5}$$

$$\mathrm{Zn(g)} + \mathrm{CO} = \mathrm{ZnO(s)} + \mathrm{C(s)} \tag{6}$$

The off-gas treatment system for the packed-bed solar reactor[8,12] was specially designed for the production of fine zinc dust by quenching the flue gases with cold off-gas recycled back after zinc-dust separation in a cyclone. The solar-produced Zn dust allows for flexible chemical storage of solar energy and can be used for the production of high-purity H_2 and CO as precursors to synthetic liquid fuels,[13–16] or for electricity generation using Zn-air batteries,[12,17] while the reoxidized Zn is recycled back to the solar reactor in the form of ZnO, thus closing the thermochemical cycle. For the industrial application of zinc as a metal commodity, however, it is advantageous to condense zinc vapor to liquid rather than solid to avoid remelting the metal for subsequent refining and casting. In the conventional ISF process, the vapor is scrubbed from the furnace off-gas with lead droplets in a lead splash condenser.[3] Zinc is thereby rapidly quenched and absorbed into molten lead, and reoxidation is mostly avoided. While several other concepts have been described in the literature,[18–21] some of which have been tested at pilot scale or commercially operated, the lead splash condenser remains the only commercial zinc condensation process in operation today. Adapting the conventional lead splash condenser in a solar thermochemical plant has several disadvantages however due to its mechanical complexity, its high operating and maintenance costs, and the health, safety, and environmental issues relating to the use of lead.[22] Furthermore, because concentrated solar energy is used instead of coke combustion as the source of high-temperature process heat for driving the carbothermal reduction, the resulting off-gas has significantly lower CO_2 content ($p_{CO_2} < 0.05$ atm; $\frac{p_{CO_2}}{p_{CO}} < 0.14$)[8] and consequently is less thermodynamically favorable toward zinc reoxidation, as it will be shown in the analysis that follows. This can facilitate the application of simpler zinc condenser concepts.

In this article, the development of an alternative zinc condenser to produce liquid zinc from the gas products evolving from the solar carbothermal reduction of ZnO is investigated. A comprehensive literature review of the kinetics of Zn(g) oxidation, and of metal vapor condensation concepts for the production of liquid metals, identified a potential alternative Zn condensation process. The technical feasibility of a proposed condensation process is assessed by the development of a transient model of simultaneous heat and mass transfer that links the competing condensation rates and kinetics of zinc vapor oxidation for solar reactor conditions. The condenser model allows the establishment of design specifications and operating conditions of a zinc condenser prototype.

ZINC VAPOR OXIDATION AND CONDENSATION

Zinc Vapor Oxidation Studies and Kinetic Models

The prevention of oxidizing conditions between a zinc producing reactor and the condensing unit is a major issue in ZnO carbothermal reduction processes such as the ISF process, and it would be similarly so for a solar zinc reactor-condenser process. As the gas temperature in the off-gas system decreases, the equilibrium of Eq. 5 is shifted to the product side favoring reoxidation of zinc vapor by CO_2. At low temperatures, reoxidation can also proceed via reaction with CO (Eq. 6) to form ZnO and elemental carbon, but the reaction rates are apparently low as minimal carbon formation has been detected in operating industrial condensers. Zinc vapor oxidation reactions have been shown to proceed heterogeneously on a solid substrate or ZnO deposited on the reaction surface.[22–32] Previous studies of Zn(g) oxidation by CO_2 carried out at temperatures between 973 K and 1273 K and partial pressures of Zn(g) in the range of 0.01–0.45 atm report reaction rates in the range of 10^{-9} mol cm^{-2} s^{-1} to 10^{-7} mol cm^{-2} s^{-1}. The kinetics of Zn(g) oxidation in CO_2-CO-N_2 mixtures were first studied for typical ISF gas compositions by Scott and Fray[24] at temperatures between 1073 K and 1203 K and $p_{Zn(g)}$ up to 0.17 atm. Zinc vapor was generated by passing a CO_2-CO-N_2 gas mixture through a packed bed of ZnO pellets and was then flown through a SiO_2 tube at a lower temperature, thereby allowing reoxidation to occur. The selected Zn(g) generation method, however, imposed a significant composition constraint ($p_{Zn(g)} \leq p_{CO_2}$). The experimental data were fitted to a reversible, second-order rate expression:

$$r'' = k_1 \cdot \left(p_{Zn(g)} p_{CO_2} - \frac{p_{CO}}{K_{eq}} \right) \tag{7}$$

where k_1 is the forward reaction rate constant and K_{eq} is the equilibrium constant for reaction (5).

Clarke and Fray[26] studied the heterogeneous oxidation of Zn(g) in CO_2-CO-Ar atmosphere at temperatures between 973 K and 1123 K and $p_{Zn(g)}$ in the range of 0.01–0.1 atm using the same experimental setup. Two distinct reaction rate regimes were identified: (I) Below 1073 K, coarse ZnO deposits were detected in the silica reactor tube and the reaction rate was proposed to be controlled by the excess $p_{Zn(g)}$:

$$r'' = k_1 \cdot \left(p_{Zn(g)} - p^{eq}_{Zn(g)}\right) \tag{8}$$

and (II) for temperatures above 1073 K and $p_{CO} > 0.2$ atm, fine-grained ZnO prevailed and the surface desorption of CO was claimed to be the rate-limiting step of the reaction:

$$r'' = k_1 \cdot \left(p_{Zn(g)} p_{CO_2} - \frac{p_{CO}}{K_{eq}}\right) \cdot \left(p_{CO} - p^{eq}_{CO}\right) \tag{9}$$

where p^{eq}_{CO} is the partial pressure of carbon monoxide at chemical equilibrium. Investigations of the Zn(g) oxidation reaction over a wider range of compositions ($p_{Zn(g)} \geq p_{CO_2}$), and at higher $p_{Zn(g)}$, were facilitated by the modified reactor-flow apparatus used by Leonard[28] and Stansbury.[29] In their study, zinc vapor was generated by saturation of a CO stream passing over a silica boat of Zn(l) and then mixed with CO_2 in a high-temperature zone to form a homogeneous reacting mixture. It was then passed through a low-temperature reactor tube where reoxidation occurred. For temperatures in the ranges of 1013–1273 K and 1243–1263 K, and Zn(g) partial pressures of up to 0.28 atm and 0.22 atm, respectively, the reaction was proposed to be independent of the partial pressure of the reacting gases and zero-order rate expressions were formulated for two temperature regimes:

$$lnr'' = 2.934 \times 10^3 \left(\frac{1}{T + 273}\right) - 1.585 \quad 765°C \leq T < 883°C \tag{10}$$

$$lnr'' = 1.807 \times 10^4 \left(\frac{1}{T + 273}\right) - 2.761 \quad 883°C \leq T \leq 1000°C \tag{11}$$

A major shortcoming of the experimental methodology is, however, the exclusion from the reaction rate analysis of the material deposited at the entrance region of the silica reactor tube. Furthermore, the possibility of ZnO forming by reaction (6) either in the vapor generation or the reaction zone is ignored by the use of CO as an inert carrier gas. Dell'Amico and See[22,23] used an alternative Zn(g) generation technique to investigate the oxidation reaction in CO_2-CO-N_2 atmosphere at compositions typical of those observed in the ISF off-gas system ($p_{Zn(g)}$, p_{CO_2}, and p_{CO} in the range of 0.04–0.12 atm, 0.10–0.17 atm, and 0.11–0.27 atm, respectively). A zinc-saturated N_2 gas stream was produced by bubbling the gas through a Zn(l) bath and passed into the zinc vapor reactor held at the selected oxidation temperature (1023–1273 K). Coarse-grained ZnO deposits of similar morphology and reaction rates of the same order of magnitude (10^{-7} mol cm^{-2} s^{-1}) as those obtained by Clarke[26] were reported. A semiempirical kinetic rate expression similar in form to Eq. 8 was proposed:

$$r'' = 9.31 \times 10^{-4} \times e^{-5610/T} \left(p_{Zn(g)} - p^{eq}_{Zn(g)}\right) \tag{12}$$

The work of Lewis and Cameron[30,31] was motivated by the absence of a kinetic rate expression at higher Zn(g) partial pressures, as most of the existing studies were carried out at typical ISF gas compositions. In their study, zinc vapor was generated by saturation of an Ar stream flowing over a sealed crucible of Zn(l), and the oxidation was investigated at temperatures in the range of 1073–1273 K and partial pressures of Zn(g) between 0.18 atm and 0.45 atm. The higher zinc content reflected gas compositions obtained during operation of plasma furnaces for the recovery of zinc from steel plant waste dusts. The reaction system was proposed to follow a three-step mechanism involving the competing reactions (5), (6), and (3), and a plug flow model was used for the formulation of an overall kinetic rate expression:

$$r'' = k_1 \cdot p_{Zn(g)} \cdot p_{CO_2} + k_2 \cdot p_{Zn(g)} \cdot p_{CO} \tag{13}$$

where k_1 and k_2 are the forward rate constants of reactions (5) and (6), respectively. At high p_{CO}/p_{CO_2} ratios, Zn(g) oxidation by CO prevailed in the system and the oxidation rate equation (Eq. 13) was reduced to the $k_2 \cdot p_{Zn(g)} \cdot p_{CO}$ term, while at low p_{CO}/p_{CO_2} ratios, the last term on the right-hand side (RHS) of Eq. 13 becomes negligible and the ZnO formation rate is proportional only to $p_{Zn(g)}$ and p_{CO_2}. Osborne et al.[32] investigated the kinetics in a Zn-CO-CO_2-N_2 system at gas compositions reflecting the ISF conditions ($p_{Zn(g)}$, p_{CO_2}, and p_{CO} in the range of 0.01–0.09 atm, 0–0.58 atm, and 0–0.55 atm, respectively) and at temperatures between 1003 K and 1023 K. The method previously used by Leonard[28] and Stansbury[29] was implemented for the generation of Zn(g). The reaction rate was found to increase with increasing partial pressure of CO, despite it being a reaction product, leading to the conclusion that the rate-limiting step of the reaction is the autocatalytic oxidation of Zn(g) by CO. A kinetic rate model was developed on a mechanistic basis. The proposed mechanism supported the adsorption of Zn(g) on the silica surface before it reacted, either directly or after forming a "Zn-CO" species, with CO_2. The mechanism was claimed to support the autocatalytic character of the reaction

and a corresponding reaction rate expression was formulated:

$$r'' = \frac{(k' + k'' \cdot p_{CO}) \cdot \left(p_{Zn(g)} p_{CO_2} - \frac{p_{CO}}{K_{eq}}\right)}{\left(1 + k''' \cdot p_{Zn(g)}\right)} \quad (14)$$

where k', k'', and k''' are reaction rate constants of individual reaction steps and K_{eq} is the equilibrium constant of reaction (5).

Figure 1 represents an equilibrium phase stability diagram for the carbothermal reduction of ZnO, including the equilibrium p_{CO_2}/p_{CO} ratio curves for the reactions Zn(g) + CO_2 = ZnO(s) + CO, Zn(l) + CO_2 = ZnO(s) + CO and 2 CO = C(s) + CO_2 at selected values of $p_{Zn(g)}$ and p_{CO}. This diagram shows regions of stability for gas and pure solid phases of ZnO and carbon. The carbothermal reduction of ZnO proceeds in the region enclosed between the equilibrium p_{CO_2}/p_{CO} curves for Zn(g) oxidation by CO_2 and the reverse Boudouard reaction. Above the equilibrium curves of Zn(g) + CO_2 = ZnO(s) + CO, zinc vapor becomes unstable and oxidation is favored. A considerable increase in the reversion temperature of reaction (2) can be observed with increasing p_{CO_2}/p_{CO} ratios at fixed $p_{Zn(g)}$. Also indicated in Fig. 1 is a summary of the experimental conditions reported in Zn(g) oxidation studies and the solar reactor conditions for representative experimental runs at ZnO:C molar ratios of 1:0.8 and 1:0.9.[7,8,10] A typical range of p_{CO_2}/p_{CO} ratios for the solar-driven process is 0.11–0.26 because of the elimination of coke combustion. Most prior studies investigated Zn(g) oxidation at considerably higher ratios. Only Lewis and Cameron[30,31] and Osborne et al.[32] conducted significant numbers of experiments at p_{CO_2}/p_{CO} ratios coinciding with typical solar reactor atmospheres. Lewis and Cameron's work also considered $p_{Zn(g)}$ in the range 0.18–0.45 atm, thus reflecting typical $p_{Zn(g)}$ values of 0.2 atm for a representative solar carbothermal reduction of ZnO at a ZnO:C molar ratio of 1:0.8.[10] Therefore, the reaction rate expression proposed by Lewis and Cameron (Eq. 13) is used in the current study.

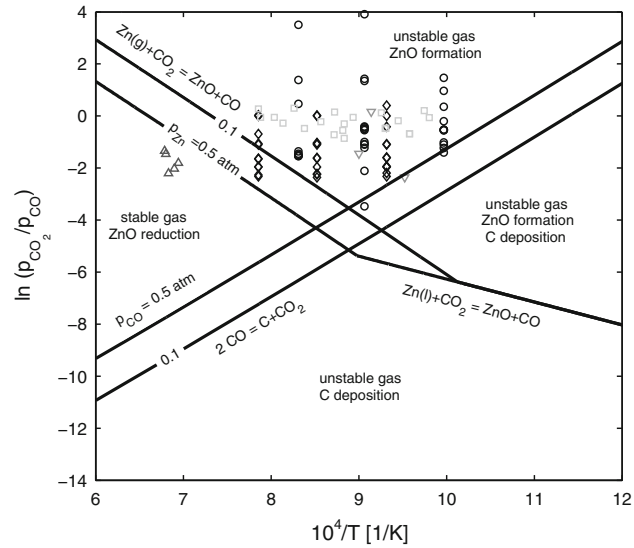

Fig. 1. Equilibrium phase stability diagram for the carbothermal reduction of ZnO at $p_{Zn(g)}$, p_{CO} = 0.1 atm and 0.5 atm. Indicated are the experimental conditions reported in zinc vapor oxidation studies and the gas atmosphere for the packed-bed solar reactor outlet for representative experimental runs at ZnO:C molar ratios of 1:0.8 and 1:0.9: Clarke and Fray[26] (▽), Dell'Amico and See[22] (□), Lewis and Cameron[30,31] (◇), Osborne et al.[32] (○), Solar reactor[7,8,10] (△).

Zinc Vapor Condensation and Industrial Condensers

Suppression of the thermodynamically favorable reoxidation reactions of Zn(g) by CO_2 and CO can be attained by rapid cooling of the gaseous products. Historically, advancements in the ZnO reduction processes and increasing zinc production rates have been the main drivers for the development of novel Zn(g) condensation techniques. For example, the reaction products of a horizontal retort furnace process,[1] comprising about 45% Zn(g) and 55% CO, would condense on the wall of surface-type fireclay condensers. This early design was suitable for the low Zn production rates (40 kg Zn/day) of a horizontal retort, but major shortcomings arose from the large number of condensers required and subsequently the high operational and maintenance costs. High-efficiency direct-contact condensation techniques became the center of interest for advanced Zn production technologies due to higher specific transfer areas, rapid transfer rates, relative simplicity of design, and lower maintenance costs. In the New Jersey Zinc Company's continuous vertical retort process[33] with a capacity of 8 tpd Zn, zinc was recovered from gas products of similar composition to a horizontal retort furnace by passing them countercurrently to a zinc splash condenser. In this arrangement, graphite rotors dipped into a Zn(l) pool created an intense shower of Zn(l) droplets to rapidly chill the furnace gases and absorb zinc vapor. The zinc pool was maintained at temperatures below 550°C through a water-cooled circulation system to keep equilibrium vapor losses to a minimum. Besides the New Jersey Zinc Process, zinc splash condenser technology has been adapted also in electrothermal[34] and plasma-arc[35] processes for zinc recovery from electric-arc furnace (EAF) dusts. Fuming of species other than zinc from the EAF feedstock however enhances the formation of heterogeneous condensation sites and, subsequently, contributes to fog and dross formation with a deleterious effect on zinc recovery. Another zinc condenser concept is the so-called "Wheaton-Najarian vacuum condenser" developed for the 2.44 m-bore electrothermic zinc furnace at Josephtown Zinc Smelter with a capacity of 20–80 tpd Zn.[36,37] This condenser recovered zinc by bubbling a mixture of Zn(g) with noncondensable gases upwardly through a Zn(l) bath enclosed in a U-tube chamber

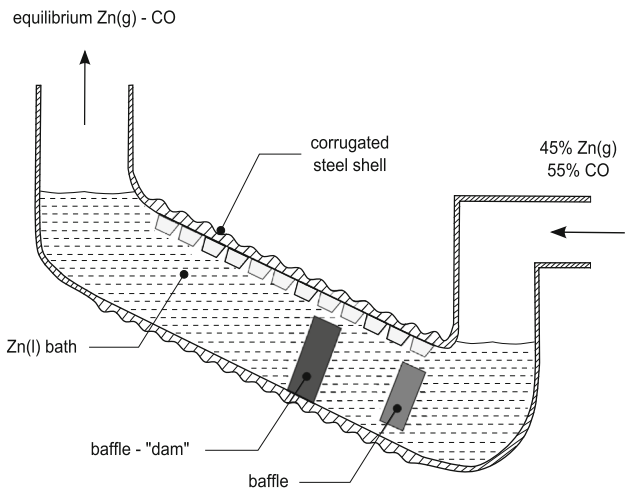

Fig. 2. Schematic of the Wheaton–Najarian vacuum condenser (based on drawings by Najarian[21]).

by suction. Brick baffles projecting normally to the inside of the roof of the condensing chamber were used to increase residence time and gas–liquid interfacial area through bubble breakup, as depicted in Fig. 2. Zinc that condensed and accumulated in the condenser was periodically tapped out. Condensation efficiency of the order of 97–98% of theoretical was obtained when keeping the Zn(l) bath temperature in the range of 480–525°C.[19–21]

The dominating pyrometallurgical Zn blast furnace process (ISF), however, required a condenser capable of handling high gas flows with low zinc concentration and of absorbing approximately 2.5 times the amount of heat absorbed by the Wheaton–Najarian (W–N) condenser per mole of Zn produced.[38] This is attributed to the heat liberated during cooling of an increased amount of noncondensable gases.[4,38] A splash condenser was developed by the Imperial Smelting Company[4] to recover zinc vapor flowing countercurrent to a liquid lead droplet shower produced by the rotation of steel impellers immersed in a bath of liquid lead. A zinc-rich phase is separated from the Zn-Pb alloy leaving the condenser at 550°C with a Zn content of 2.26 wt.% by exploiting an immiscibility gap of the Zn-Pb binary system. The liquid stream is cooled down to 440°C, where the solubility limit of 2.02 wt.% is reached, and liquid zinc separates as a layer over Pb(l). The liquid zinc is tapped out and the liquid lead is recirculated to the condenser inlet for recovery of fresh Zn(g). The lead splash condenser technology thus requires a continuous supply of large amounts of liquid lead ranging between 300 and 400 tonnes per tonne of Zn produced to operate. Although this condenser has high operational and maintenance costs, and it uses lead that suffers from critical health, safety, and environmental issues, it remains the only commercially used zinc condensation process. Besides primary zinc production processes, the ISP lead splash condenser technology has been used in processes for zinc recovery from steel plant dusts and zinc-containing slag. Recovery of 98.4 wt.% pure zinc from lead-blast furnace slags using the Enviroplas process[39] has been successfully demonstrated at a 5.6 MVA scale.[40] Several other condensation technologies have been proposed for the recovery of Zn(l) from a body of molten lead.[41–45] A multicompartment combined Zn(l)- and Pb(l)-splash condenser concept has been trialed to reduce the amount of Pb(l) recirculated.[46] A lead-spray zinc condenser has been developed by SKF Plasma Technologies AB for zinc recovery from high-zinc-containing carbon steel dusts, but operation was terminated due to economic reasons after switching from processing carbon steel dusts to low-zinc-containing (<6 wt.%) alloy-steel dusts. Other zinc condensers such as of Solnordal et al.[18] experimentally investigated the feasibility of using a fluidized bed of zircon sand to condense zinc from smelter off-gases as a solid. They reported the rapid cooling of the gas–vapor mixtures from about 1200–500°C within 8 ms and Zn recovery exceeding 90%. The solid zinc condenser product, however, has disadvantages because it needs to be remelted for subsequent refining and casting of ingots.

In the solar reactor process,[7,8] reaction gases also need to be rapidly quenched from the thermodynamically stable gas outlet temperature of 1473 K to temperatures where the kinetic rate of Zn reoxidation is slow. Major shortcomings for the application of the conventional lead splash condenser in a solar thermochemical plant arise from its size, mechanical complexity, and other issues described previously. Bubbling gas condensation through a bath of Zn(l) like the W–N vacuum condenser has advantages of simplicity (no moving mechanical parts), intensity (smaller size), and no need of a secondary liquid metal phase. Solar reactor off-gas products are characterized by high p_{CO}/p_{CO_2} ratios compared with those in an ISF, and the oxidation potential can be further decreased by operation with increased amount of carbon in the feedstock (ZnO:C molar ratios lower than 1:0.8) to produce gas compositions similar to the electrothermic furnace. A decrease in the flow rate of the inert carrier gas (N_2) allows for a significant reduction of the heat liberated during Zn(g) absorption and reduces the problem of heat dissipation that was reported to be the most significant shortcoming of the W–N condenser.[20,21] The W–N condenser design was not adopted for wide commercial application as it was initially developed for handling low gas volumes and gas atmospheres with low oxidation potential, and it was thus less suited to ISF conditions. However, with trends toward new technologies such as arc furnaces for zinc production and their formation of high concentration, lower volume Zn(g)-CO streams, molten zinc bath condensers should be reconsidered. This does also apply to future new zinc processes such as

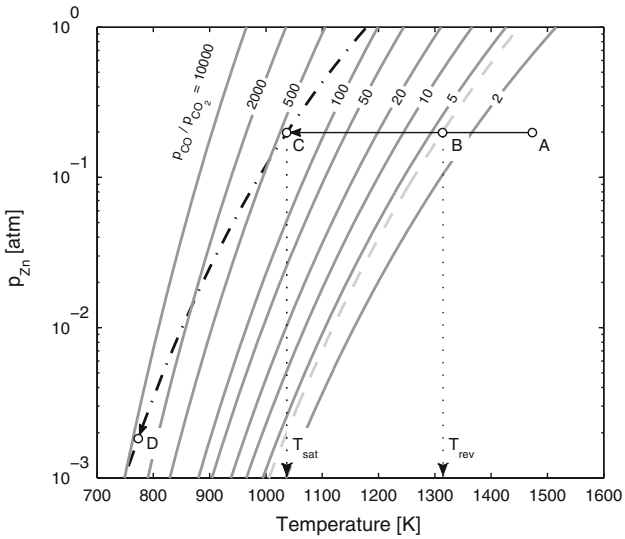

Fig. 3. Variation of the Zn vapor pressure and equilibrium Zn(g) partial pressure for reaction (5) at p_{CO}/p_{CO_2} ratios in the range of 2–10,000 along with points (A, B, C, D) relevant to the operation of a 10 kW_{th} packed-bed solar reactor.[10]

the solar-driven thermochemical plants considered in this study. Therefore, the molten zinc bath condenser concept is chosen in the current study aiming at producing liquid Zn from the product gas evolving from the solar carbothermal reduction of ZnO.

The operating conditions for the solar zinc reactor-condenser process can be characterized by a plot of the variation of Zn vapor pressure and equilibrium Zn(g) partial pressure for reaction (5) at p_{CO}/p_{CO_2} ratios in the range 2–10,000,[47] along with points relevant to the operation of a 10 kW_{th} packed-bed solar reactor,[10] as shown in Fig. 3. Typical solar reactor gas products containing 19.9% Zn(g) leave the reactor at 1473 K and a p_{CO}/p_{CO_2} ratio of 3.8 (point A). This gas composition corresponds to the highest oxidation potential measured during typical experimental runs at ZnO:C molar ratios of 1:0.8 and 1:0.9 and is used as the base case scenario in the current study. Reoxidation of Zn(g) by CO_2 is thermodynamically unfavorable until the reversion temperature of 1314 K (point B) is reached, while condensation will commence only below the apparent saturation temperature of 1037 K (point C). Equilibrium condensation upon further cooling of the gases to the temperature of the Zn(l) bath at 773 K (point D) follows the line CD. Thus, rapid quenching of the gas–vapor mixture should minimize the residence time and prevent ZnO formation in the temperature range between 1314 K and the kinetically unfavorable temperature of 773 K for the reversion reactions to occur.

CONDENSATION MECHANISM OF VAPOR BUBBLES

The key process in a molten zinc bath condenser is the condensation of Zn(g) from gas–vapor bubbles, the initial composition being that of the solar reactor process gas. The condensation and collapse of vapor bubbles in liquid baths has been extensively investigated at different degrees of subcooling, i.e., where the bath is maintained at temperatures below the apparent saturation temperature of the vapor. At high degrees of subcooling, bubble collapse is controlled by the inertia forces of the surrounding liquid and proceeds rapidly while no laminar boundary layer can be observed.[48–51] Heat transfer through the vapor–liquid interface governs the process at moderate temperature differences. Heat-transfer-controlled condensation of bubbles has been previously experimentally studied in miscible[52–58] and immiscible[59] liquids. Bubble condensation Nusselt numbers have been derived capable of describing the dynamic nature of the liquid–vapor interface, as opposed to the case of convective heat transfer from a solid object. A critical evaluation of Nusselt correlations for vapor bubble condensation in subcooled flows is provided by Rabello and Buongiorno.[60] The effect of noncondensable gases on the bubble collapse rate was investigated by Jacobs and Major[61] and Ullmann and Letan.[62] The dimensionless Jacob number, defined as the ratio of sensible to latent heat absorbed during the vapor–liquid phase change, is used to define the limits of the inertia-controlled and heat-transfer-controlled regimes of condensation:

$$Ja = \frac{\rho_l \cdot c_{p,l} \cdot \left(T_s^* - T_\infty\right)}{\rho_v \cdot \Delta h_{fg}} \tag{15}$$

where T_s^* is the apparent saturation temperature, T_∞ is the temperature in the bulk liquid, $c_{p,l}$ is the specific heat capacity of the liquid, Δh_{fg} is the enthalpy of evaporation, and ρ_l and ρ_v are the density of the liquid and the vapor, respectively. Chen and Mayinger[54] specified interfacial heat transfer as rate limiting up to $Ja = 80$, while a transition region of mixed effects was identified before entering the liquid inertia-controlled regime ($Ja > 100$). Besides the temperature of the liquid bath, Ja varies with the partial pressure of the condensing vapor in the gas mixture when noncondensable gases are present. As the condensation proceeds, the fraction of noncondensable gases increases, thereby inducing a decrease in the apparent saturation temperature. Figure 4 shows the effect of the fraction of noncondensable gases on the apparent saturation temperature of Zn(g) and on the Jacob number during condensation of the gas–vapor mixture at selected temperatures of the Zn(l) bath. Inertia forces in the liquid phase govern condensation of a solar reactor gas–vapor mixture initially containing 19.9% Zn(g) in a highly subcooled Zn(l) bath maintained at 500°C, as indicated by the initial $Ja = 600$. Transition to the heat-transfer controlled regime is reached at $\Delta T_{sub} = T_s^* - T_\infty = 55$ K, corresponding to 99.3% content of noncondensable gases in the gas–vapor mixture.

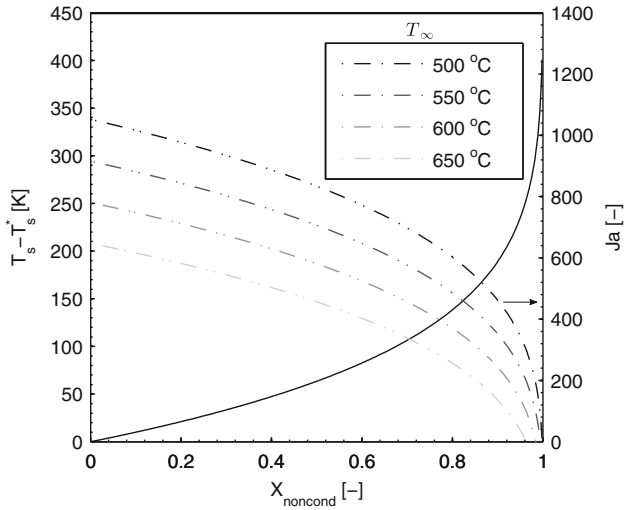

Fig. 4. Effect of the fraction of noncondensable gases on the apparent saturation temperature of Zn(g) and the Jacob number (*Ja*) for selected temperatures of the Zn(l) bath.

FORMULATION OF HEAT- AND MASS-TRANSFER MODEL

Governing Equations

A simplified, zero-dimensional transient heat and mass transfer model of a single bubble rising through a Zn(l) bath was developed to investigate the competing condensation rates and kinetics of oxidation of zinc vapor for a wide range of gas compositions. Neglect of the heat and mass transfer resistance within the bubble is justified by vigorous toroidal circulation of gas inside the bubble by virtue of the viscous drag of the outer fluid as described by Garner and Hammerton.[63] In the case of condensing bubbles, circulation is further enhanced by the shrinking effect of the vapor–liquid interface. With the assumptions of (I) no interaction between individual bubbles, (II) constant liquid bulk temperature due to high thermal conductivity of the liquid phase, (III) constant relative velocity between bubbles and liquid, (IV) constant total pressure of 1 bar throughout, (V) reaction rate expressions as proposed by Lewis and Cameron for the reoxidation of Zn(g), and (VI) reactions occurring in the thermodynamically favorable regions according to Fig. 3, the mass conservation equation is:

$$\frac{\mathrm{d}m_\mathrm{b}}{\mathrm{d}t} = M_\mathrm{Zn} \cdot r_\mathrm{Zn(g),cond} \tag{16}$$

where m_b is the mass of the bubble containing zinc vapor, noncondensable gases and the solid species involved in the reactions (3), (5), and (6). The RHS term accounts for the mass of the condensate exchanged with the liquid bath defined by the condensation molar source multiplied by the molar weight of Zn. The conservation equation of species k in the bubble is:[64]

$$\frac{\mathrm{d}m_k}{\mathrm{d}t} = M_k \cdot r_k \tag{17}$$

where $r_k = \sum_{j=1}^{3} r_{k,j}$ for CO, CO_2, N_2, ZnO, and C, and $r_\mathrm{Zn(g)} = \sum_{j=1}^{3} r_\mathrm{Zn(g),}j + r_\mathrm{Zn(g),cond}$ for Zn(g). The summation accounts for the mass change of species k at the three individual steps involved in the Zn(g) oxidation reaction mechanism. The energy conservation equation expressed in terms of the sensible enthalpy $h_\mathbf{s}$ is:[65]

$$m_\mathrm{b} c_\mathrm{p,eff} \frac{\mathrm{d}T_\mathrm{b}}{\mathrm{d}t} + \sum_{k=1}^{6} r_k h_\mathrm{s,k} = -hA_\mathrm{b}\left(T_\mathrm{b} - T_\mathrm{Zn(l)}\right) - r_\mathrm{Zn(l),cond} h_\mathrm{s,Zn(l)} + r_\mathrm{Zn(l),cond} \Delta h^o_{gf} + \sum_{j=1}^{3} r_j \Delta h^o_\mathrm{rxn,}j \tag{18}$$

where $c_\mathrm{p,eff}$ is the effective specific heat capacity, T_b is the temperature of the gas–vapor mixture, $h_{\mathrm{s},k}$ is the sensible enthalpy of species k, h is the convective heat-transfer coefficient, $r_\mathrm{Zn(l),\ cond}$ is the molar production rate of liquid zinc, and A_b is the interfacial area calculated assuming a spherical bubble. The second term on the RHS of Eq. 18 represents the energy of mass exchanged with the liquid phase, while the two last terms denote the heat of condensation and the heat of reactions (5), (6), and (3) at standard conditions. Different correlations are applied for the interfacial heat-transfer coefficient depending on the physical phenomena taking place and the controlling mechanism of condensation. The Hughmark correlation,[66] initially developed for flows around rigid spheres, is employed during cooling of the gas–vapor mixture to the apparent saturation temperature (line segment AC in Fig. 3):

$$h = \begin{cases} \frac{k_\mathrm{l}}{D_\mathrm{b}}\left(2 + 0.6\mathrm{Re}_\mathrm{b}^{1/2}\mathrm{Pr}_\mathrm{l}^{1/3}\right) 0 \le \mathrm{Re}_\mathrm{b} \le 776 \\ \frac{k_\mathrm{l}}{D_\mathrm{b}}\left(2 + 0.27\mathrm{Re}_\mathrm{b}^{0.62}\mathrm{Pr}_\mathrm{l}^{1/3}\right) \mathrm{Re}_\mathrm{b} \ge 776 \end{cases} \tag{19}$$

where $\mathrm{Re}_\mathrm{b} = \frac{u_\mathrm{rel} D_\mathrm{b}}{\nu_\mathrm{l}}$ is the bubble Reynolds number, u_rel is the relative velocity between gas and liquid, D_b is the bubble diameter, and ν_l, k_l, and Pr_l represent the kinematic viscosity, thermal conductivity, and Prandtl number of the liquid, respectively. In the inertia-controlled regime the kinetic theory of gases can be used for the vapor–liquid interface. The heat-transfer coefficient is then obtained using the Hertz–Knudsen–Shrage equation[67] corrected for a curved interface:[68,69]

$$h = \frac{4}{4 - 3K_c}\left(\frac{1}{2\pi M_\mathrm{Zn} R}\right)^{1/2} \left\{ K_\mathrm{C} \frac{p_\mathrm{Zn(g)}}{T_\mathrm{b}^{1/2}} - K_E \frac{p_\mathrm{Zn(l)}}{T_\mathrm{Zn(l)}^{1/2}} \right\} \cdot \frac{\Delta h_{gf}}{\left(T_\mathrm{b} - T_\mathrm{Zn(l)}\right)} \tag{20}$$

where $p_{Zn(l)}$ is the saturation partial pressure of zinc vapor at $T_{Zn(l)}$, and K_C and K_E are the condensation and evaporation coefficients. K_C is defined as the ratio of incident vapor molecules absorbed by the liquid phase to the molecules impinging onto the liquid–vapor interface, and K_E is the ratio of molecules entering the vapor phase to the molecules leaving the liquid phase. The simplification $K_C = K_E = 0.96$ is used as was measured for the condensation coefficient at a solid–liquid Zn interface by Rapp et al.[70]

In the heat-transfer controlled condensation regime the following correlation proposed by Chen and Mayinger[54] for $Re_b \leq 10{,}000$ and $2 \leq Pr_l \leq 15$ is implemented:

$$h = \frac{k_l}{D_b}\left(0.185 Re_b^{0.7} Pr_l^{1/2}\right) \tag{21}$$

Numerical Method and Code Verification

An adaptive time-stepping technique is employed for the entire calculation procedure to enhance the robustness of the code and to achieve the desired solution accuracy with minimum computational effort.[71] The automatic control of the time step is based on the estimation of the local truncation error associated with the time integration scheme. Considering an ordinary differential equation of the form:

$$\frac{dy}{dt} = F(t, y(t)) \tag{22}$$

an estimate of the local error τ at $t + \Delta t$ is obtained by applying the explicit Euler integration scheme using two time steps of different size, Δt and $\Delta t/2$:

$$y_{t+\Delta t} = y_t + \Delta t \cdot F(t, y_t) \tag{23}$$

$$y_{t+\frac{\Delta t}{2}} = y_t + \frac{\Delta t}{2} \cdot F(t, y_t) \tag{24}$$

$$y'_{t+\Delta t} = y_{t+\frac{\Delta t}{2}} + \frac{\Delta t}{2} \cdot F\left(t + \frac{\Delta t}{2}, y_{t+\frac{\Delta t}{2}}\right) \tag{25}$$

$$\tau_{t+\Delta t} = y'_{t+\Delta t} - y_{t+\Delta t} \tag{26}$$

The local error estimate is compared with a prescribed local error tolerance value τ_{TOL} to either accept the current time step size or calculate the optimal time step Δt^*:

$$\Delta t* = 0.9 \Delta t \frac{\tau_{TOL}}{\tau_{t+\Delta t}} \tag{27}$$

where 0.9 is a damping factor used to decrease the risk of rejection of the next time step. The local error tolerance value τ_{TOL} is set equal to 5×10^{-3} to ensure an acceptable accuracy of the solution with minimum computational effort. A study has been conducted to facilitate the selection of an appropriate value for the local error tolerance. Values below 10^{-2} have been shown to have a negligible effect on the solution accuracy. The corresponding plots are omitted for brevity.

The correct implementation of the numerical method has been assessed by performing a code verification study using the method of manufactured solutions.[72] The assessment of the implementation is based on conducting a time-step refinement study in which the global error between the numerical solution and an "exact" manufactured solution is evaluated as the time step size is reduced. Thus, the code verification study has been conducted using a fixed time step size for the entire calculation procedure rather than an adaptive time step. The order of accuracy of the numerical method is determined from the rate at which the numerical solution tends to the "exact" manufactured solution. A correct implementation of the numerical method can be ensured when the actual order of accuracy for the individual terms in the governing equations approaches the nominal order of accuracy in the asymptotic range of convergence. For Eqs. 16–18, the actual order of accuracy approaches unity with decreasing time step size when applying the explicit Euler integration scheme, which indicates the correct implementation of the numerical method. The corresponding plots are omitted for brevity.

RESULTS AND DISCUSSION

In the following, the modeling results are described and discussed based on process conditions typical for the solar carbothermal ZnO reduction process.

Results

The temperature of the Zn(l) bath, the initial bubble diameter, the relative velocity between bubbles and liquid, as well as the fraction of noncondensable gases in the vapor–gas mixture are the main parameters affecting the total process time and condensation efficiency. Bath temperatures in the range of 500–650°C were investigated to allow efficient operation of the condenser while maintaining an adequate margin above the melting point to avoid solidification. Although the majority of studies on gas bubbles rising in liquid baths involve sparging or submerged lance injection, these techniques entail a high risk of clogging by solid products formed during Zn(g) reoxidation and are not considered practical for the zinc vapor reactor application. Pumping or suction of the vapor–gas mixture through a Zn(l) bath in a similar manner to

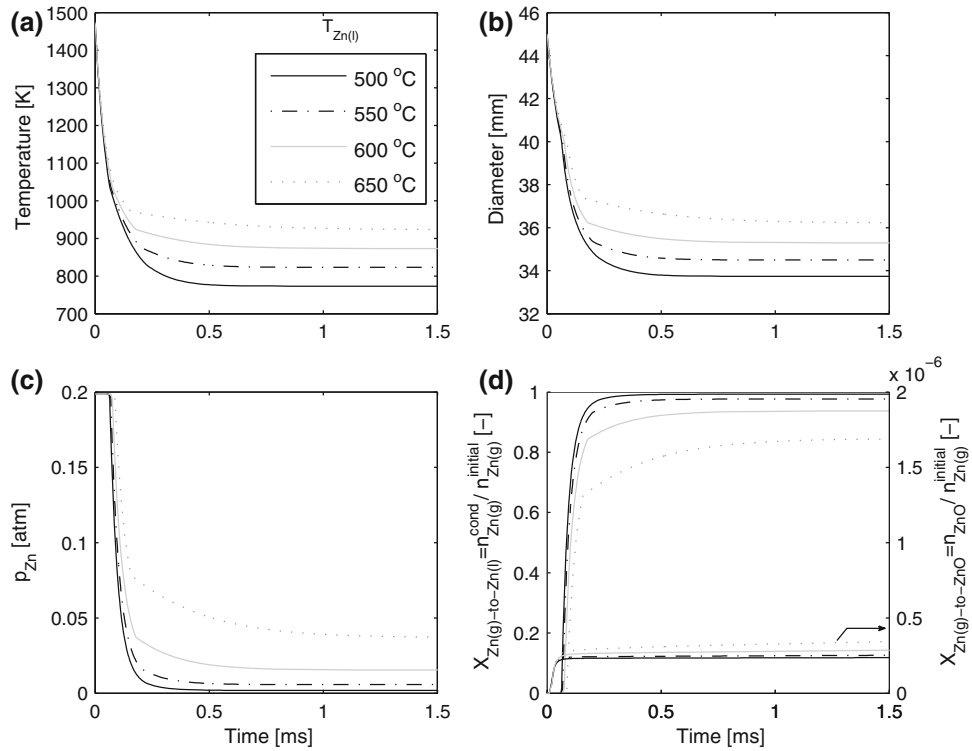

Fig. 5. Variation of the (a) gas temperature, (b) bubble diameter, (c) Zn(g) partial pressure, and (d) chemical conversion of Zn(g)-to-Zn(l) and Zn(g)-to-ZnO for a bubble with an initial diameter of 45 mm and 80.1% noncondensable gases rising at 0.11 m s^{-1} in a Zn(l) bath maintained in the temperature range of 500–650°C.

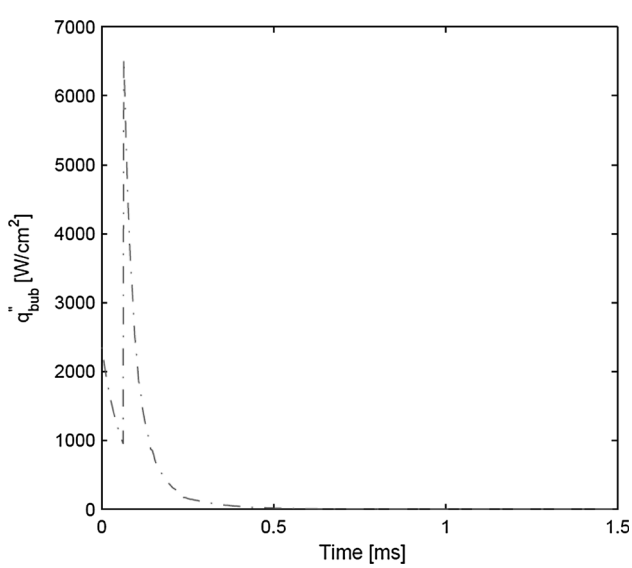

Fig. 6. Heat flux from a bubble with an initial diameter of 45 mm and 80.1% noncondensable gases rising at 0.11 m s^{-1} in a Zn(l) bath maintained at 500°C.

the W–N vacuum condenser favors the formation of large gas bubbles. In line with the findings of Haberman and Morton,[73] bubble diameters in the range of 10–80 mm are considered in the current study.

Haberman and Morton[73] further identified increasing terminal rise velocities with increasing bubble size. For bubbles in the 10–80 mm range, the terminal velocity is independent of the properties of the surrounding liquid and can be obtained according to:[73]

$$u_{\mathrm{term}} = 1.02\sqrt{g\frac{D_{\mathrm{b}}}{2}} \tag{28}$$

Relative velocities between bubbles and liquid in the range between 0.02 m s^{-1} and 0.2 m s^{-1}, the terminal rise velocity for a 10 mm-diameter bubble, were therefore studied in the current work. To investigate the effect of the presence of noncondensable gases in the mixture, the initial fractions of noncondensable gases were varied between 0.535 and 0.801. These conditions are typical for the 10 kW_{th} packed-bed solar reactor[10] and correspond in this experimental setup to inert carrier gas (N_2) mass flow rates between 0.5 and 5 L_N min^{-1} (liters at normal conditions; mass flow rates are calculated at 273 K and 1 bar), respectively. These conditions were used as the basis for modeling.

The variation of the gas temperature, the bubble diameter, the Zn(g) partial pressure, and the chemical conversions of Zn(g) to Zn(l) and ZnO as a function of time is shown in Fig. 5a–d, respectively, for a bubble with an initial diameter of 45 mm and 80.1% noncondensable gases rising at 0.11 m s^{-1} in a Zn(l) bath at temperatures in the range of

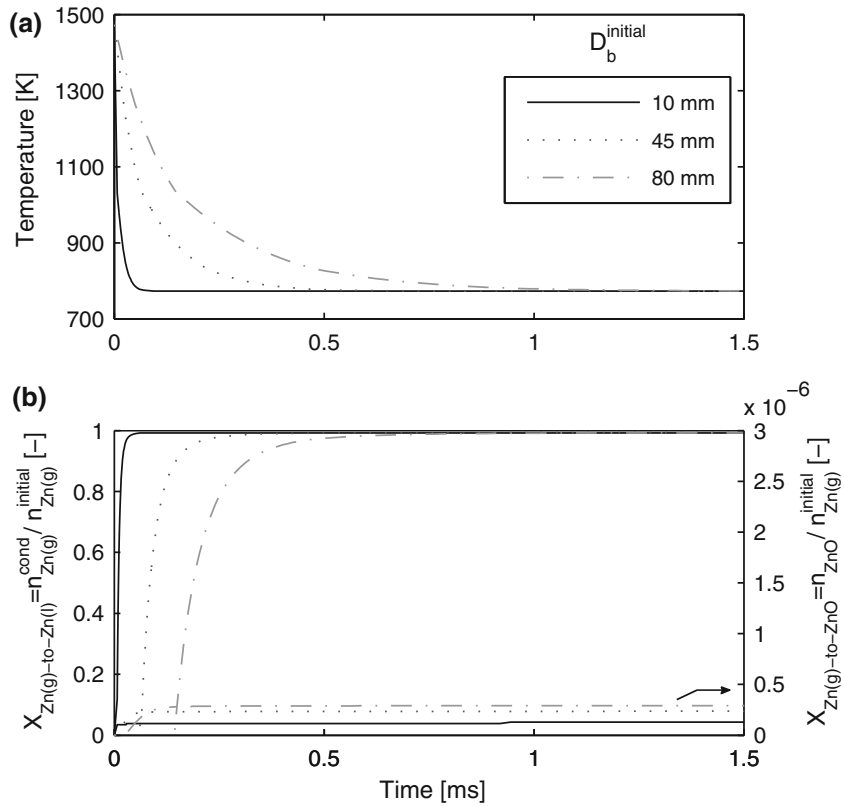

Fig. 7. Effect of the initial bubble diameter on the heat and mass transfer rates as illustrated by the variation of temperature and chemical conversions for a bubble with an initial content of 80.1% noncondensable gases rising at 0.11 m s^{-1} in a Zn(l) bath maintained at 500°C.

500–650°C. The gas temperature drops monotonically to reach the corresponding Zn(l) bath temperature within less than 1 ms. Higher heat-transfer rates are observed with decreasing bath temperatures owing to the higher thermodynamic driving forces. The obvious change in curvature in the temperature curves, which for $T_{Zn(l)}$ = 600°C is clearly identifiable at 0.2 ms, is attributed to the transition from inertia-controlled to heat-transfer-controlled condensation regimes. A notable increase in the final bubble diameter from D_b = 33.7 mm at $T_{Zn(l)}$ = 500°C to D_b = 36.2 mm at $T_{Zn(l)}$ = 650°C is obtained due to the nonlinear increase of the equilibrium Zn(g) losses with temperature, as indicated in Fig. 5b and c. Figure 5d reveals that rapid quenching of the gas–vapor mixture to temperatures, where the formation of ZnO is kinetically hindered, enables the suppression of the reversion reactions of Zn(g) by CO_2 and CO and facilitates high Zn(l) yields. Conversion of Zn(g) to Zn(l) increases from 0.845 at $T_{Zn(l)}$ = 650°C to 0.992 at 500°C, whereas only a small fraction of Zn(g) entering the condenser is predicted to form ZnO. The fraction of reversion $X_{Zn(g)\text{-to-}ZnO}$ is in the range of 2.4×10^{-7} to 3.6×10^{-7}.

The heat flux from a bubble with an initial diameter of 45 mm, and 80.1% noncondensable gases, rising at 0.11 m s^{-1} in a Zn(l) bath maintained at 500°C is shown in Fig. 6. The initial drop in the heat flux curve corresponding to cooling without condensation (line segment AC in Fig. 3) is followed by a heat flux peak of 6500 W cm^{-2} as the gas–vapor mixture reaches the apparent saturation temperature of 1037 K and condensation commences. The notable decrease in the heat flux at temperatures below 1037 K is attributed to the decreasing partial pressure of Zn(g) and, hence, mass transfer driving force. Large amounts of heat are released from the condensing bubble surface as a result of both the rapid Zn(g) condensation and the high enthalpy of condensation. Heat flux values shown in Fig. 6 are comparable to fluxes of 1896–3564 W cm^{-2} reported in Gunther's cinematographic study[74] of the mechanism of highly subcooled (ΔT_{sub} = 245–256°C) nucleate boiling of water.

The effect of the initial bubble diameter on the heat and mass transfer rates for a bubble with an initial content of 80.1% noncondensable gases rising at 0.11 m s^{-1} in a bath maintained at 500°C is shown in Fig. 7 by plotting the variation of the gas temperature and chemical conversions as a function of time. An increase of the initial diameter from 10 mm to 80 mm induces a two orders of magnitude increase in the time required to reach the apparent saturation temperature and thermal equilibrium due to the decrease of the surface-area-to-volume ratio. For a 10-mm-diameter bubble, condensation commences after 7 μs to reach a $X_{Zn(g)\text{-to-}Zn(l)}$ of 0.992

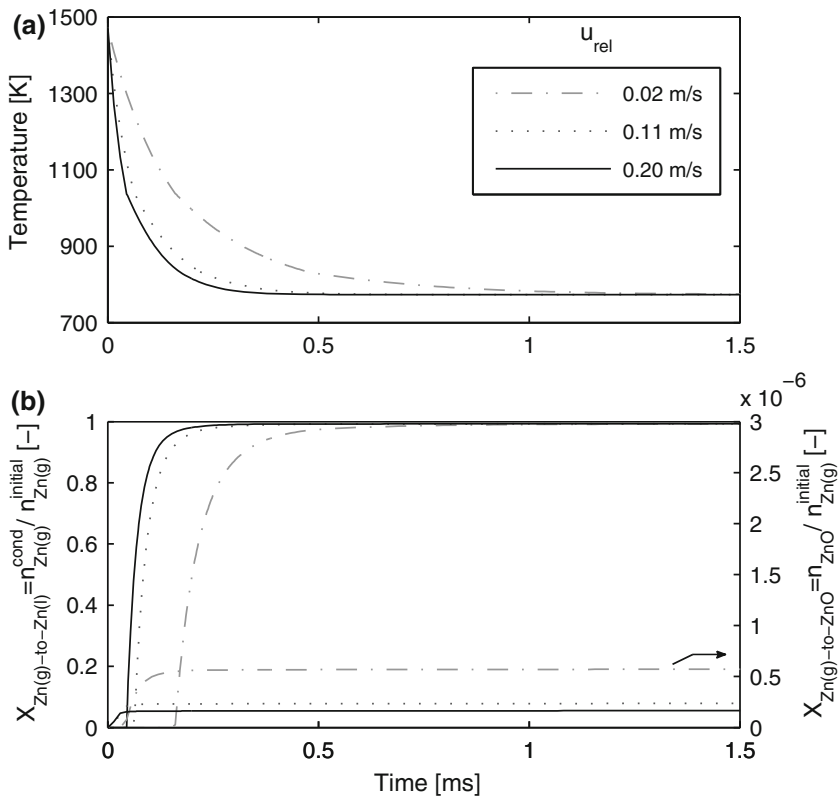

Fig. 8. Effect of the relative velocity between gas bubbles and liquid on the heat and mass transfer rates as illustrated by the variation of temperature and chemical conversions for a bubble with an initial diameter of 45 mm and initial content of 80.1% noncondensable gases rising in a Zn(l) bath maintained at 500°C.

after 60 μs, whereas a 80-mm-diameter bubble requires 1.12 ms to reach the same conversion. Lower heat-transfer rates with increasing bubble diameter result in an increase of the asymptotic $X_{\text{Zn(g)–to-ZnO}}$ conversion from 1.3×10^{-7} to 2.9×10^{-7} due to the longer residence time of the gas–vapor mixture at temperatures favoring ZnO formation. An increase in the gas–liquid relative velocity results in similar trends as a decrease in the initial bubble diameter, as shown in Fig. 8 for a bubble with an initial diameter of 45 mm. An order of magnitude increase in the relative velocity reduces the time required to reach a $X_{\text{Zn(g)-to-Zn(l)}}$ of 0.992 from 1.32 ms to 0.39 ms due to the enhanced heat and mass transfer, whereas the asymptotic $X_{\text{Zn(g)–to-ZnO}}$ conversion decreases from 5.7×10^{-7} to 1.7×10^{-7}.

Figure 9 shows the effect of the molar fraction of noncondensable gases on the time variation of the bubble diameter and the chemical conversions of Zn(g) to Zn(l) and ZnO for a bubble with an initial diameter of 45 mm, rising at 0.11 m s^{-1} in a Zn(l) maintained at 500°C. The fraction of noncondensable gases in the bubble controls the thermodynamic driving force in the condensation process by affecting the Zn(g) partial pressure and, consequently, the apparent saturation temperature. Thus, higher fractions of noncondensable gases induce a decrease in the shrinking rate of the bubble, as depicted in Fig. 9a. The increase of the final bubble diameter from 29.5 mm to 33.7 mm with increasing initial content of noncondensable gases is attributed to the volume occupied by the additional amount of N_2 in the gas–vapor mixture. The fraction of noncondensable gases exhibits a negligible effect on the $X_{\text{Zn(g)-to-Zn(l)}}$ conversion (Fig. 9b), which varies between 0.992 and 0.998 at initial contents of 80.1% and 53.5% noncondensable gases, respectively. In contrast, $X_{\text{Zn(g)-to-ZnO}}$ conversion increases by an order of magnitude from 2.37×10^{-7} to 1.03×10^{-6} at a lower content of noncondensable gases due to the first-order dependence of the reversion reaction rates on the partial pressures of Zn(g), CO, and CO_2.

The effect of liquid bath temperature and fraction of noncondensable gases on the $X_{\text{Zn(g)-to-Zn(l)}}$ conversion is shown in Fig. 10. The notable decrease in the $X_{\text{Zn(g)-to-Zn(l)}}$ conversion with increasing liquid zinc bath temperature is attributed to the nonlinear increase of the equilibrium vapor losses with temperature. The variation of the $X_{\text{Zn(g)-to-Zn(l)}}$ conversion between 0.992 and 0.998 at initial molar contents of 80.1% and 53.5% noncondensable gases illustrates a negligible effect of the fraction of noncondensable gases on the condensation efficiency for a highly subcooled liquid bath maintained at 500°C. On the contrary, an increase in the content of

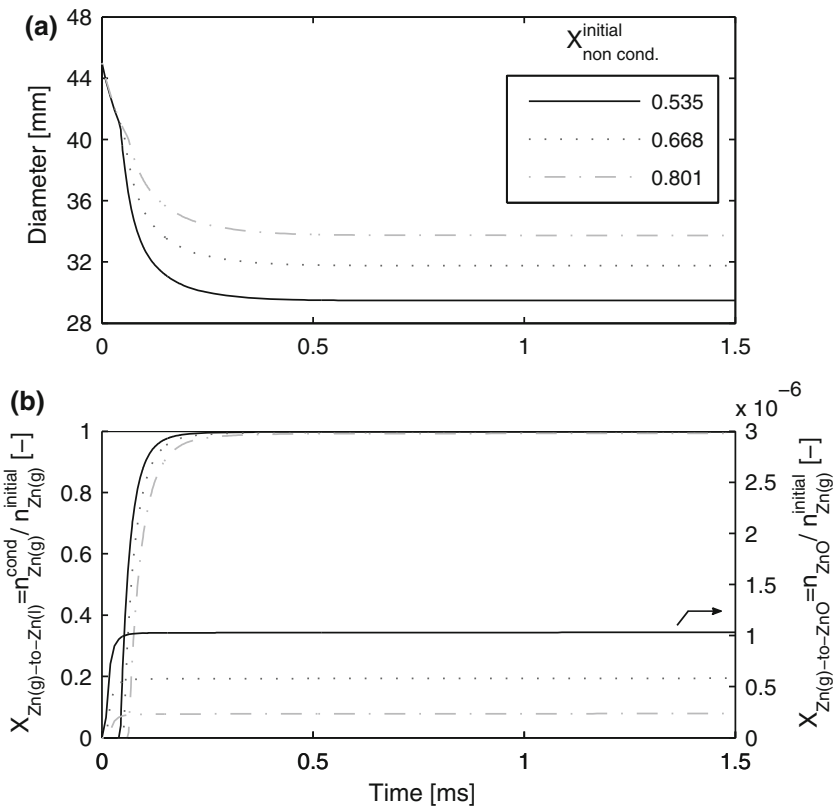

Fig. 9. Effect of the molar fraction of noncondensable gases on the shrinking rate of the bubble and the time variation of the Zn(g)-to-Zn(l) and Zn(g)-to-ZnO chemical conversions for a bubble with an initial diameter of 45 mm rising at 0.11 m s^{-1} in a Zn(l) bath maintained at 500°C.

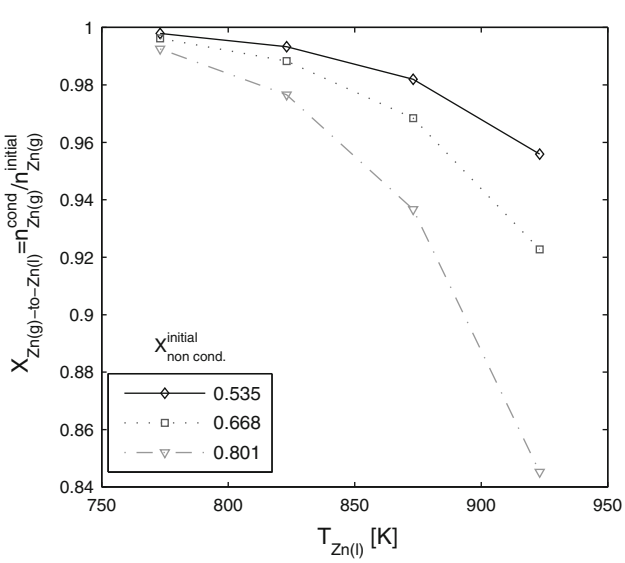

Fig. 10. Effect of the Zn(l) bath temperature and the fraction of noncondensable gases on the conversion of Zn(g) to Zn(l).

noncondensable gases in the gas–vapor mixture from 53.5% to 80.1% induces a strong nonlinear decrease in the Zn(g)-to-Zn(l) conversion from 0.956 to 0.845 for condensation in a liquid bath maintained at 650°C, which is attributed to the effect of their presence on the Zn(g) partial pressure and the apparent saturation temperature.

Discussion

Numerical heat- and mass-transfer modeling demonstrates that zinc vapor reoxidation reactions proceed considerably slower than condensation, thus preventing a considerable decrease of the Zn(g) partial pressure in the undersaturated vapor region due to oxidation by CO_2 and CO. The results suggest the technical feasibility of the molten zinc bath condenser concept for zinc gas condensation from high concentration Zn(g)-CO streams such as from a reactor for the solar carbothermal reduction of ZnO. The higher condensation rates obtained with decreasing initial bubble diameter and increasing gas–liquid relative velocity confirm the use of baffles in the Zn(l) bath to prevent coalescence of individual bubbles, enhance bubble breakup, and improve heat transfer such as that used in the W–N condenser. Furthermore, the negligible effect of fraction of noncondensable gases on the condensation efficiency predicted for a highly subcooled liquid bath at 500°C is supported by observations on the operation of the pilot–scale W–N condenser mounted at the outlet of the electrothermic zinc furnace at the Josephtown Zinc Smelter. Rapid and almost complete condensation of zinc vapor was reported for

operation at liquid bath temperatures in the range of 500–525°C, irrespective of the amount of accompanying noncondensable gases.[20]

CONCLUSION

A zinc condenser concept involving bubbling of gas–vapor products of the solar carbothermal reduction of ZnO through a subcooled Zn(l) bath has been proposed to rapidly condense Zn(g) to Zn(l) and suppress reoxidation of Zn(g) by CO_2 and CO. A simplified mass- and heat-transfer model was developed to investigate the competing condensation rates and kinetics of oxidation of zinc vapor at solar reactor conditions. A $X_{\text{Zn(g)-to-Zn(l)}}$ conversion of 0.992 was predicted for a 45-mm-diameter bubble containing 80.1% noncondensable gases in a liquid bath maintained at 500°C, whereas successful suppression of the reversion reactions was demonstrated ($X_{\text{Zn(g)-to-ZnO}} = 2.4 \times 10^{-7}$). A notable decrease in the $X_{\text{Zn(g)-to-Zn(l)}}$ conversion with increasing temperature due to equilibrium vapor losses supports the operation of a vacuum condenser at low temperatures by efficiently dissipating the large amounts of heat released during the rapid condensation process. The condensation rates were significantly enhanced by a decrease of the initial bubble diameter and increase of the relative velocity between the bubbles and liquid bath. A pronounced decrease of the Zn(l) yield with increasing fractions of noncondensable gases in the mixture suggests operation with a minimal amount of inert gases to maintain a predicted $X_{\text{Zn(g)-to-Zn(l)}}$ above 0.95 in a wide liquid bath temperature range and to minimize the heat liberated in the process.

ACKNOWLEDGEMENTS

We gratefully acknowledge the financial support by the Swiss Federal Office of Energy (contract SI/500660-01) and by European Research Council under the European Union's ERC Advanced Grant (SUNFUELS - No. 320541).

REFERENCES

1. C.H. Mathewson, *Zinc: The Science and Technology of the Metal, Its Alloys and Compounds* (London: Reinhold Publication Corporation, 1959).
2. C.H. Cotterill and J.M. Cigan, eds., *AIME World Symposium on Mining & Metallurgy of Lead & Zinc: Extractive Metallurgy of Lead and Zinc* (Englewood: American Institute of Mining, Metallurgical, and Petroleum Engineers, 1970).
3. R.J. Sinclair, *The Extractive Metallurgy of Zinc* (Victoria: Australasian Institute of Mining and Metallurgy, 2005).
4. S.W.K. Morgan, *Bull. Inst. Min. Met.* 67, 553 (1957).
5. A. Steinfeld, *Energy* 22, 311 (1997).
6. T. Osinga, U. Frommherz, A. Steinfeld, and C. Wieckert, *J. Sol. Energy Eng.* 126, 633 (2004).
7. S. Kräupl, U. Frommherz, and C. Wieckert, *J. Sol. Energy Eng.* 128, 8 (2006).
8. C. Wieckert, U. Frommherz, S. Kräupl, E. Guillot, G. Olalde, M. Epstein, S. Santén, T. Osinga, and A. Steinfeld, *J. Sol. Energy Eng.* 129, 190 (2007).
9. M. Epstein, G. Olalde, S. Santén, A. Steinfeld, and C. Wieckert, *J. Sol. Energy Eng.* 130, 014505 (2008).
10. N. Tzouganatos, R. Matter, C. Wieckert, J. Antrekowitsch, M. Gamroth, and A. Steinfeld, *JOM* 65, 1733 (2013).
11. S. Kräupl and A. Steinfeld, *J. Sol. Energy Eng.* 123, 237 (2001).
12. C. Wieckert, M. Epstein, G. Olalde, S. Santén, and A. Steinfeld, *Encyclopedia of Electrochemical Power Sources* (New York: Elsevier, 2009), pp. 469–486.
13. A. Steinfeld, *Sol. Energy* 78, 603 (2005).
14. K. Wegner, H.C. Ly, R.J. Weiss, S.E. Pratsinis, and A. Steinfeld, *Int. J. Hydrog. Energy* 31, 55 (2006).
15. A. Stamatiou, P.G. Loutzenhiser, and A. Steinfeld, *AIChE J.* 58, 625 (2012).
16. D. Weibel, Z.R. Jovanovic, E. Gálvez, and A. Steinfeld, *Chem. Mater.* 26, 6486 (2014).
17. K.F. Blurton and A.F. Sammells, *J. Power Sources* 4, 263 (1979).
18. C.B. Solnordal, G.W. Jensen, and F.R.A. Jorgensen (Paper presented at Minprex 2000: International Congress on Mineral Processing and Extractive Metallurgy, 11–13 September 2000, Melbourne, VIC, The Australasian Institute of Mining and Metallurgy (AusIMM) Publication Series), pp. 485–491.
19. G.F. Weaton and H.K. Najarian, U.S. patent US2070101 A (1937).
20. H.K. Najarian, *Trans. Am. Inst. Min. Metall. Eng.* pp. 161 (1944).
21. H.K. Najarian, *Trans. Am. Inst. Min. Metall. Eng.* 212, 493 (1958).
22. M. Dell'Amico and J.B. See, *Pyrometallurgy* 87, 305 (1987).
23. M. Dell'Amico (Master's thesis, The University of Newcastle, 1989).
24. J.V. Scott and D.J. Fray, *Advances in Extractive Metallurgy*, ed. M.J. Jones (London: Institution of Mining and Metallurgy, 1972), pp. 95–105.
25. A. Cox and D.J. Fray (Paper presented at the Yazawa International Symposium on Metallurgy and Materials Processing: Principles and Technology, 2003), pp. 95–105.
26. J.A. Clarke and D.J. Fray, *J. Mater. Sci.* 13, 1921 (1978).
27. J.A. Clarke, *Chem. Ind.* 6, 1 (1979).
28. R.L. Leonard (Master's thesis, Colorado School of Mines, 1985).
29. K.L. Stansbury (Master's Thesis, Colorado School of Mines, 1987).
30. L.A. Lewis and A.M. Cameron, *Metall. Mater. Trans. B* 26, 911 (1995).
31. L.A. Lewis and A.M. Cameron, *Metall. Mater. Trans. B* 26, 919 (1995).
32. J.M. Osborne, W.J. Rankin, D.J. McCarthy, and D.R. Swinbourne, *Metall. Mater. Trans. B* 32, 37 (2001).
33. E.H. Bunce and E.C. Handwerk, *Trans. AIME* 121, 427 (1936).
34. T. Pedersen, J.A. Aune, and R.A. Cundall, *Lead-Zinc 90* (Warrendale: The Minerals, Metals & Materials Society, 1990), pp. 857–879.
35. C.D. Chapman, P.M. Cowx, J.K. Pargeter, and D.N. Pocklington, *Recycl. Met. Mater.* (London: Institution of Mining and Metallurgy, 1990), pp. 47–55.
36. G.F. Weaton, H.K. Najarian, and C.C. Long, *Trans. TMS-AIME* 159, 141 (1944).
37. C.C. Long, *J. Met.* 17, 351 (1965).
38. L. Gourtsoyannis (Master's thesis, McGill University, 1972).
39. A.F. Schoukens, M.A. Abdel-Latif, M.J. Freeman, and N.A. Barcza (Paper presented at the 1996 Electr. Furn. Conference Proceedings, 1996), pp. 341–351.
40. A.F.S. Schoukens, G.M. Denton, and R.T. Jones (Paper presented at the International Symposium on Recycling of Metals and Engineered Materials, Point Clear, AL, 1995), pp. 857–868.
41. P. Neve, U.S. patent US2238819 A (1941).
42. S. Robson and L.J. Derham, U.S. patent US2464262 A (1949).
43. S. Robson and L.J. Derham, U.S. patent US2671725 A (1954).
44. L.J. Derham, U.S. patent US2886309 A (1959).

45. M.I. Hoschke, U.S. patent US5215572 A (1993).
46. S. Robson, U.S. patent US2473304 A (1949).
47. O. Kubaschewski and C.B. Alcock, *Metallurgical Thermochemistry* (New York: Pergamon Press, 1979).
48. L. Rayleigh, *Philos. Mag. Ser.* 6, 94 (1917).
49. M.S. Plesset and A. Prosperetti, *Ann. Rev. Fluid Mech.* 9, 145 (1977).
50. A.D. Okhotsimskii, *Int. J. Heat Mass Transf.* 31, 1569 (1988).
51. S.G. Bankoff and R.D. Mikesell, *Chem. Eng. Prog.* 55, 95 (1959).
52. L.W. Florschuetz and B.T. Chao, *J. Heat Transf.* 87, 209 (1965).
53. D.D. Wittke and B.T. Chao, *J. Heat Transf.* 89, 17 (1967).
54. Y.M. Chen and F. Mayinger, *Int. J. Multiph. Flow* 18, 877 (1992).
55. O. Zeitoun, M. Shoukri, and V. Chatoorgoon, *J. Heat Transf.* 117, 402 (1995).
56. G.R. Warrier, N. Basu, and V.K. Dhir, *Int. J. Heat Mass Transf.* 45, 3947 (2002).
57. H. Kalman, *Int. J. Heat Mass Transf.* 46, 3451 (2003).
58. S.-J. Kim and G.-C. Park, *Int. J. Heat Mass Transf.* 54, 2962 (2011).
59. H. Kalman, *Int. J. Heat Mass Transf.* 49, 2391 (2006).
60. G. Rabello dos Anjos and J. Buongiorno, *Bubble Condensation Heat Transfer in Subcooled Flow Boiling at PWR Conditions: A Critical Evaluation of Current Correlations* (Cambridge: Massachusetts Institute of Technology, 2013).
61. H.R. Jacobs and B.H. Major, *J. Heat Transf.* 104, 487 (1982).
62. A. Ullmann and R. Letan, *J. Heat Transf.* 111, 1060 (1989).
63. F.H. Garner and D. Hammerton, *Chem. Eng. Sci.* 3, 1 (1954).
64. T. Poinsot and D. Veynante, *Theoretical and Numerical Combustion*, 2nd ed. (Philadelphia: R.T. Edwards Inc., 2005).
65. S. Skogestad, *Chemical and Energy Process Engineering* (Boca Raton: CRC Press, 2009).
66. G.A. Hughmark, *AIChE J.* 13, 1219 (1967).
67. R.W. Schrage, *A Theoretical Study of Interphase Mass Transfer* (New York: Columbia University Press, 1953).
68. R. Marek (Ph.D. thesis, Technical University of Munich, 1996).
69. R. Marek and J. Straub, *Int. J. Heat Mass Transf.* 44, 619 (2001).
70. R.A. Rapp, J.P. Hirth, and G.M. Pound, *J. Chem. Phys.* 34, 184 (1961).
71. G. Söderlind and L. Wang, *J. Comput. Appl. Math.* 185, 225 (2006).
72. P. Knupp and K. Salari, *Verification of Computer Codes in Computational Science and Engineering*, 1st ed. (Boca Raton: Chapman and Hall/CRC Press, 2002).
73. W.L. Haberman and R.K. Morton, *Trans. Am. Soc. Civ. Eng.* 121, 227 (1956).
74. F.C. Gunther, *Trans ASME* 73, 115 (1951).